Marine and Petroleum Geology 96 (2018) 602–614

Contents lists available at ScienceDirect

Marine and Petroleum Geology

journal homepage: www.elsevier.com/locate/marpetgeo

Research paper

Genesis and growth of a carbonate Holocene wedge on the northern Little Bahama Bank

Kelly Fauquembergue[a,*], Emmanuelle Ducassou[a], Thierry Mulder[a], Vincent Hanquiez[a], Marie-Claire Perello[a], Emmanuelle Poli[b], Jean Borgomano[c]

[a] Université de Bordeaux, CNRS UMR5805 EPOC, allée Geoffroy St Hilaire, CS 50023, 33615 Pessac Cedex, France
[b] Projet "Carbonates", Exploration & Production SCR/RD, Total S.A., CSTJF, Avenue Larribau, 64000 Pau, France
[c] Aix-Marseille Université, CNRS UMR7330 CEREGE, 3, Place Victor Hugo, 13331 Marseille Cedex 3, France

ARTICLE INFO

Keywords:
Carbonate slope
Bahamas
Holocene
Off-bank transport
Meltwater pulses
Hurricanes
Cold fronts
Density cascading

ABSTRACT

The study focuses on the sedimentary dynamics at the transition between the modern Bahamas carbonate platform and related adjacent slopes and deeper environments. A Holocene carbonate sedimentary wedge is developed at the edge of the carbonate platform extending along the northern Little Bahamas Bank (LBB; Bahamas). The transition area between the platform and the wedge shows superposed terraces. The Holocene wedge thickness varies from 0 to 35 m. Its surface is dominated by homogeneous, fine-grained, soft sediments. It lies on a Pleistocene substratum and fills depressions corresponding to lowstand erosional surfaces. On the uppermost slope, this wedge represents the main depocenter of fine-grained bank-derived sediments since the last bank flooding.

Twelve gravity cores were sampled from this wedge and allow the identification of both the processes that can supply this wedge and the wedge evolution based on content analyses and 19 radiocarbon ages.

At present, particle export from the LBB margins mostly occurs during episodes of winter cold fronts but also occurs during hurricanes. Evidence of hurricane impact in the sedimentary record is suggested by the recovery of two laminated sequences showing both decreasing sedimentation rates and varying velocities during platform export. The local morphology of the platform edge allows the better sorting and export of sediments according to the presence of tidal outlets and sediment sorting on the wedge. However, because no ooids from tidal deltas located on the platform edge were found in cores, tidal currents are probably not energetic enough to both mobilize and export sediment, even if tide–induced currents may help the export of fine-grained carbonate particles remobilized by either cold fronts or hurricanes on the platform and upper slope.

The formation of the wedge started at 13.6 ± 3.5 kyr cal BP following the meltwater pulse 1 A. It was supplied by shallow environment-derived particles produced on four narrow terraces between 60 and 20 mbsl after meltwater pulses. Since the LGM (Last Glacial Maximum), terrace formation seems to correspond to periods of sea-level stillstands and wedge formation, whilst escarpments correspond to periods of high rates of rising sea-level due to meltwater pulses. The main period of wedge growth started around 6.5 ± 0.9 kyr cal BP, when sea level finally reached the platform margins. The maximum flooding period around 4 kyr cal BP is characterized by the highest contents of aragonite needles exported from the platform.

1. Introduction

Modern carbonate sedimentary systems sourced by tropical factories represent good analogues of ancient carbonate environments and allow a connection between sediment facies and depositional processes. In modern carbonate environments, the tropical factory mainly involves shallow carbonate platforms and platform margins and is restricted to a narrow area on the Earth's surface. At a geological scale, it has been more widespread, especially during greenhouse Earth periods where it extends to middle-latitude areas. In ancient carbonate systems, very little is known about the sediment transfer zones from the shallow carbonate factory to the slope and deeper environments. Recently, Holocene wedges were recognized in carbonate systems (Glaser and Droxler, 1991; Zinke et al., 2003), especially on Bahamian uppermost slopes (Betzler et al., 2014; Mulder et al., 2017; Rankey and Doolittle, 2012; Wilber et al., 1990). Bahamian Holocene wedges are located just

* Corresponding author.
E-mail address: kelly.fauquembergue@gmail.com (K. Fauquembergue).

https://doi.org/10.1016/j.marpetgeo.2018.05.013
Received 14 January 2018; Received in revised form 25 April 2018; Accepted 18 May 2018
Available online 19 May 2018
0264-8172/

downslope from platform margins, can record many environment changes including platform flooding and have the potential to supply more distal slopes. Wilber et al. (1990) proposed the storm-related suspended mud and leeward drift of whiting events as major supply mechanisms for the sediment forming this Holocene wedge. Then, Wilson and Robert (1995) estimated the outsized larger effects of winter cold fronts on sediment suspension and off-bank transport. Cold fronts initiate a thermohaline circulation that exports sediment from the shelf to the slope. This hypothesis was validated by Betzler et al. (2014).

The deposition and distribution of sediment exported off the bank is controlled by the along-slope Florida current (Betzler et al., 2014); hence, the GBB Holocene wedge was interpreted as a "periplatform drift". On the northern Little Bahama Bank (LBB) windward margin, another Holocene wedge was recently recognized by Rankey and Doolittle (2012), who made a preliminary survey to describe the uppermost slope morphology and concluded that this wedge was not markedly impacted by the bottom current. Mulder et al. (2017) imaged the wedge at deeper water depths than Rankey and Doolittle (2012) and over a large part of the margin. Mulder et al. (2017) showed that the wedge was discontinuous in front of small submarine channels supplied by tidal passes (Fig. 2) and concluded that present-day off-bank export was the result of two processes: (1) tidal current acceleration (tidal flushing) following the resuspension of fine-grained carbonate on the lagoon after hurricanes or storms, and (2) export along the whole margin by density cascading supplying the Holocene wedge. Process (1) is a temporary source process and occurs over very short periods of time (hours to days), whilst process (2) occurs simultaneously over the whole platform margin and over longer periods of time (several days). Although the export through tidal passes and channels is beginning to be understood (Rankey and Reeder, 2011; Reeder and Rankey, 2009, 2008), the timing and processes of the formation of the Holocene wedge through density cascading are not accurately understood. In this paper, we propose providing more insight about the formation of this wedge using lithological and compositional descriptions and establish a significant Holocene stratigraphic framework using a set of cores.

2. Geological settings

2.1. Environmental settings

The northern Little Bahama Bank (LBB) is an open ocean windward margin (Fig. 1; Hine et al., 1981; Hine and Neumann, 1977) settled in a high-wave-energy area. It is subject to easterly to northerly winds and waves (Fig. 1); (Hine and Neumann, 1977). Hine and Neumann (1977) demonstrated that two-thirds of all storms that affect the main ooid and coarse-grained shoals along the margin, such as the active Lily Bank, generate a net bankward flux. Shallow bank depressions (called "re-entrants" or "cuts"; Hine and Neumann, 1977; Mulder et al., 2017) were formed between reef discontinuities during the Holocene due to a large bankward flow during the last acceleration of sea-level rise (Hine and Neumann, 1977), which stabilized approximately 4 kyr BP ago (Boardman, 1988). These discontinuities formed tidal passes directly connecting the platform to the uppermost slope (Mulder et al., 2017a). Flow acceleration induced by the reduced section in reentrants increases daily tidal velocities, which can then reach 1 m/s (Reeder and Rankey, 2009). The tidal accretionary bars along tidal channels formed shoals and small emerged banks. Coarse-grained (ooids or bioclasts) ebb and flood deltas were built at the landward and oceanward mouths of the tidal passes, where tidal velocity is reduced because of the increase of the flow section (Reeder and Rankey, 2008). Shoal morphologies created by sediments bypassing reentrants indicate a flood-dominated margin (Rankey et al., 2006). The combination of tides, swell, storm-induced waves and winds creates a net bankward energy flux (Mullins et al., 1979). Hence, off-bank sediment transport towards the slope is mainly reduced (Mullins et al., 1979). However, a minor portion of platform sediments manages to bypass the northern margins: series of canyons developed on the northern LBB slopes (Mulder et al., 2012; Tournadour et al., 2017) are lined by terraces that have recorded off-bank periplatform ooze export during the Quaternary. Chabaud et al. (2015) described the deposits related to this off-bank transport in sediment cores and demonstrated that the LBB northern slopes have been supplied by platform sediments since at least MIS 11. The main processes that are suggested to supply the periplatform area from the bank are density cascading (Wilson and Robert, 1995) and hurricanes. Hurricanes have been especially frequent along Bahamian coasts since 6 kyr BP according to Toomey et al. (2013). Those events are recorded along the GBB mid-slope as centimetric layers made of coarse-grained particles that increase local sedimentation rates. The role of hurricanes in off-bank transport is evidenced by satellite images (Rankey et al., 2004). More recently, a satellite image of hurricane Matthew shows that fine-grained particles can be exported further away from the platform margin, up to ~10 km (Fig. 1). Density cascading takes place during winter Bahamian cold fronts. Cold fronts bring dry cold air masses above the LBB. This refreshes shallow platform water masses. Moreover, when cold fronts overlie a water mass, the water mass temperature decreases, reducing evaporation, but the post-front conditions (increasing air temperature faster than water mass temperature) highly enhance water evaporation and increase salinity. Hence, increasing salinity and decreasing temperature increase the platform water mass density. Higher density initiates an off-bank thermohaline circulation that carries suspended sediments (Fig. 1). This way, shelf-derived sediments are deposited deeper on the slope. Currently, Florida experiences ~23 winter cold fronts (Hardy and Henderson, 2003). The Holocene wedge is the most important sediment accumulation extending along the uppermost slope at present. The LBB Holocene wedge on the uppermost slope was investigated by Rankey and Doolittle (2012) and Mulder et al. (2017). These authors described this formation as located below a terraced escarpment, highlighting past sea-level stillstands. It is made of periplatform-ooze that fills Pleistocene substratum depressions ranging from 0 m thick between depressions to 35 m thick on the central part of the wedge. It extends from 170 mbsl to 360 mbsl, forming a transition area between the platform margin and the upper slope (Tournadour et al., 2017).

2.2. Northern LBB sediments

Bahamian platforms are considered as almost pure carbonate systems (Traverse and Ginsburg, 1966). Only 0–3.4% of sediments comprise siliciclastic grains supplied by winds (Swart et al., 2014). At the platform located upstream of the study site, Enos (1974) described four sediment types (Fig. 2): (1) grainstones along the platform margin and (2) packstones on the back of the grainstone barrier. They are both formed by skeletal grains (coral debris, fragmented benthic foraminifera, *Halimeda* flakes, seagrass fragments, *Penicillus* fragments, and bivalve shells including conch and other gastropods; Rankey and Reeder, 2011; Reeder and Rankey, 2009). (3) Ooids are found in tidal deltas. Ooids are rare off the shoals and are stacked around the highest-energy environments, such as on decreasing current velocity areas (~0.6 m/s) surrounding reentrants (Reeder and Rankey, 2009). (4) Peloids are the most abundant type of particles in the lowest current-velocity areas (< 0.4 m/s), mainly on the edges of tidal deltas (Reeder and Rankey, 2009). They are found in the southwestern part of the study area, on the back of the grainstone barrier. Platform production induced large amounts of mud that are exported from Bahamian platforms (Wilson and Robert, 1995). In the < 4 μm grain-size fraction, the grains are mostly made of small aragonite needles, nano grains of calcite and coccoliths (Gischler et al., 2013).

At bathymetries of deeper than 400 mbsl, the slope sediments are rich in planktonic grains. Chabaud et al. (2015) defined the composition of the slope environment along the western part of the LBB. It is mainly made of skeletal grains (including planktonic foraminifera,

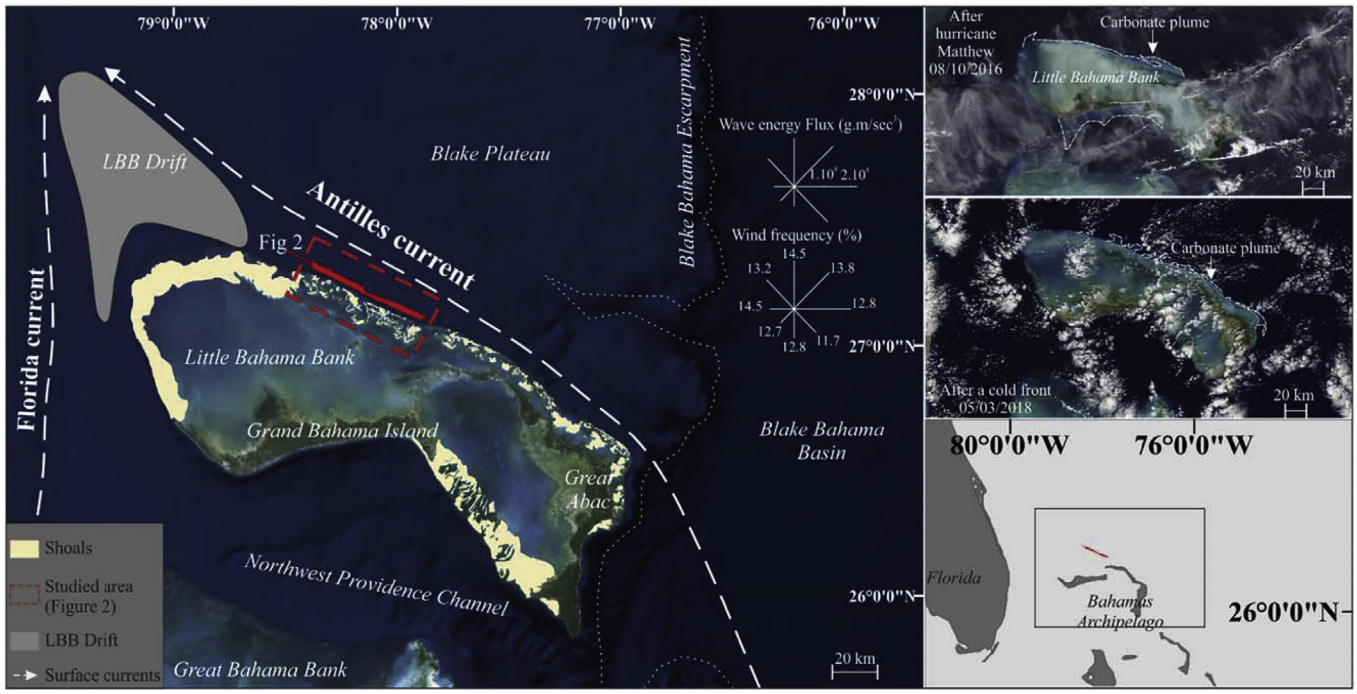

Fig. 1. Location of the study area. Wind frequency and wave energy flux (Hine and Neumann, 1977) and surface current directions (Chabaud et al., 2015; Johns, 2011; Lantzsch et al., 2007; Tournadour et al., 2017). Satellite images of LBB after Hurricane Matthew and cold fronts show carbonate plumes exporting platform-derived sediment towards the adjacent slopes (https://worldview.earthdata.nasa.gov).

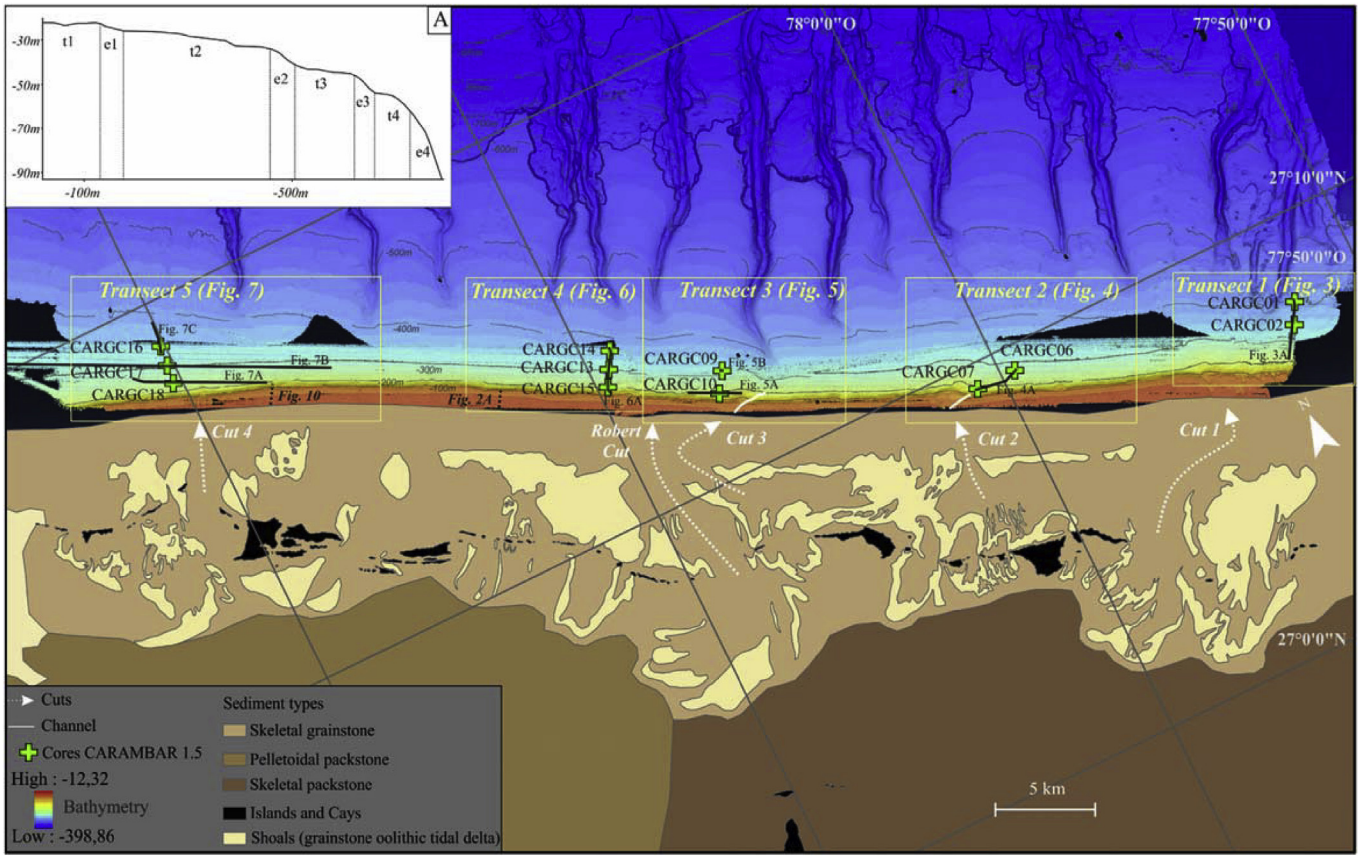

Fig. 2. Map of data combination from CARAMBAR 1.5 and CARAMBAR cruises ((Mulder et al., 2017, 2012); from red to blue colours) and platform facies (Enos, 1974), modified by Tournadour et al. (2015). Cores are indicated by green crosses and transects by black lines. Dashed white arrows indicate pathways of sediment export from the platform through tidal cuts. Fig. 2A is exported from Mulder et al. (2017). (For interpretation of the references to colour in this figure legend, the reader is referred to the Web version of this article.)

pteropods, and a few benthic foraminifera), peloids, nodules concentrated during glacial periods, and mud composed of a carbonate matrix made of aragonite needles and few coccoliths.

2.3. Oceanic shallow currents

The Carambar 1.5 cruise (Mulder, 2014) recorded three vertical sound-velocity profiles, which allowed the delimitation of two water masses on the study site. The first corresponds to a mixing layer and extends from 75 to 150 mbsl (Rosenthal et al., 1997). The second water mass is located just below and probably corresponds to the Antilles Current, which is the main current flowing northwestward in the area (Johns, 2011). It can reach approximately 6 Sv (Sv = 10^6 m^3/s) between 800 and 1000 mbsl in the eastern part of the Bahamas (Meinen et al., 2004). At the northwesternmost part of the Bahamas, it connects with the Florida Current to form the Gulf Stream (Fig. 1; Mullins et al., 1988). At the current merging, a large drift (Hine et al., 1981) called the "Little Bahama Drift" formed (Fig. 1; Chabaud et al., 2015; Tournadour et al., 2015). The influence of the Antilles Current is supposed to be limited to less than 25 cm/s in the CARAMBAR 1.5 study area (Johns, 2011).

3. Material & methods

3.1. Bathymetry and high-resolution seismic data

The study area is located on the northern Little Bahama Bank (Fig. 2) and was investigated during the CARAMBAR 1.5 cruise in November 2014, on board the R/V F.G. Walton Smith. A total of 150 km^2 of multibeam echosounder bathymetry data (Teledyne Reson Seabat 7125) and 1120 km of high-resolution seismic profiles (3.5 kHz, Knudsen Chirp 3260, resolution) were collected during the cruise.

3.2. Sedimentological data and methods

To study sedimentary processes and deposition features on the wedge, 12 gravity cores were collected using a 5.82-m calypso piston corer (diameter = 7.62 cm) for a cumulative length of 50.78 m (Table 1). Cores are located on the upper (more proximal), middle (intermediate) and lower (more distal) parts of the wedge along 5 transects numbered from 1 to 5 in a westward direction and covering a longshore distance of 57 km (Fig. 2). Each transect is ~3 km long. A few cores are located at a cut outlet (CARGC07 and CARGC10). CARGC09 is in the middle of a small depression. Analyses were performed in the University of Bordeaux-CNRS, EPOC laboratory. Visual descriptions and photographs of each core section were obtained to help lithological descriptions. Core density was analysed using the SCOPIX X-ray image-processing tool (Migeon et al., 1998).

Continuous semi-quantitative analyses of selected major elements were realized using an XRF–AVAATECH Core Scanner. A measurement step of 1 cm was used along the cores. The elements used in this study are strontium (Sr, 30 kV, 15 s acquisition time) and calcium (Ca, 10 kV, 10 s acquisition time). The Sr/Ca ratio is used to evaluate the presence of aragonite in sediments as an indicator of shallow-water sources (Croudace et al., 2006; Droxler, 1983) in which Sr can substitute for Ca and shallow-water organisms are enriched in strontium.

Grain-size measurements have been performed on 898 sediment samples using a laser particle size analyser (Malvern Mastersizer, 2000). Core CARGC07 contained grains coarser than 2 mm, which is the maximum size of Malvern Mastersizer measurements. Hence, for this core, grain size measurements were realized on the muddy/silty part of samples after sieving to isolate sandy grains (> 63 μm). This way, the proportions of sand-sized grains were established by sieving weights. The proportion of > 150 μm grains was elaborated using Malvern Mastersizer measurements.

To analyse the different types of particles, sediment samples were washed and sieved at 63 μm. Samples were collected for every 2 kyr cal BP according to the age model described below. The sand fraction (> 63 μm) was studied under a binocular reflected light microscope, and the silt and clay-size fraction (< 63 μm) was observed on smear slides with an optical microscope. Thin sections were realized on the most spectacular sedimentary sequences after sediment induration using the methodology published by Zaragosi et al. (2006).

3.3. Age model and base of the wedge

To establish the age models of cores, 19 radiocarbon dates were measured on planktonic foraminifera and pteropod tests (Table 2). Measurements were done using the ARTEMIS accelerator mass spectrometer at the CEA centre in Saclay (Gif-Sur-Yvette, France). The obtained dates were calibrated using the MARINE 13 curve (Reimer et al., 2013) and the Calib ^{14}C Calibration Program.

Sedimentation rates were calculated from the zero-depth (top of cores) down to the depth of the uppermost ^{14}C measurement, then, when available, in between two successive ^{14}C measurements. The spacing between two measurements was measured with a maximum accuracy of 1 cm, while the uncertainty of the ^{14}C age was below 0.04 kyr for all measurements (Table 2). For two cores (CARGC09 and CARGC14), a ^{14}C measurement was made at the top of the core and each measurement led to an age younger than 0.2 kyr, so that whenever the age was measured from the zero-depth down to the first ^{14}C measurement, an uncertainty on the time-lapse of 0.24 kyr was considered. Two ^{14}C measurements were made on cores CARGC01, 02, and 07, and three measurements were made on core CARGC15, allowing us to compute intermediate sedimentation rates for each core and different time-lapses. An average sedimentation rate was then computed by

Table 1
Location and details of cores used for this study (Carambar 1.5 cruise) and corresponding grain sizes analyses. * correspond to sediments too coarse to obtain D50 values with the Malvern 2000 laser microgranulometer.

Cores	Latitude	Longitude	Depth (-m)	Transect number	Position on the wedge	Core length (m)	D50 min (μm)	D50 max (μm)	< 20 μm (%)	20–150 μm (%)	> 150 μm (%)
CARGC01	27°7932′	77°51,990′	389	1	Middle wedge	1.64	12.637	36.371	50,98	45,26	3,76
CARGC02	27°7444′	77°52,275′	340		Lower wedge	5.25	9.163	33.979	51,95	43,05	5,01
CARGC06	27°09,404′	77°59,622	275	2	Lower wedge	5.10	12.712	37.794	47,03	46,03	6,94
CARGC07	27°09,394′	78°00,752	177		Upper wedge	4.56	*	*	20,01	20,46	59,53
CARGC09	27°12,481′	78°06,748	308	3	Lower wedge	4.83	9.163	71.261	48,24	47,76	4,00
CARGC10	27°12,014′	78°07,081	190		Upper wedge	4.46	15.023	61.173	41,86	49,13	9,02
CARGC13	27°13,706	78°09,484	306	4	Middle wedge	4.94	16.106	54.533	40,20	50,87	8,93
CARGC14	27°14,106	78°09,241	360		Lower wedge	3.96	15.719	36.383	44,00	50,08	5,92
CARGC15	27°13,33′	78°09,72	203		Upper wedge	4.68	6.446	202.099	45,44	37,45	19,50
CARGC16	27°13,33′	78°09,72	342	5	Lower wedge	2.37	8.223	35.262	48,62	46,52	4,86
CARGC17	27°13,33′	78°09,72	306		Middle wedge	4.12	9.36	115.891	42,79	49,88	7,33
CARGC18	27°18,003′	78°20,240	252		Upper wedge	4.87	7.993	25.547	55,95	25,77	18,28

Table 2
Radiocarbon dating information and results. Dates elaborated using the bulk of planktonic foraminifera and pteropods are illustrated by a *, and ** illustrates a core bottom – wedge bottom distance that is too difficult to estimate because of the highly variable topography at this location. Bottom ages of cores that reached the bottom are in bold (age estimation without using seismic extrapolation).

Core	Sample depth in core (m)	Lab code (SacA-)	^{14}C Ages (BP)	Calibrated ages (Marine 13 curve, cal BP)	Mean sedimentation rates (cm/kyr)	Bottom wedge age (yrs cal BP)
CARGC01	0.51	45990	1590 ± 35*	1156	52 ± 14	**4.4 ± 0.8**
CARGC01	0.80	45992	1970 ± 35*	1528		
CARGC02	0.54	48028	615 ± 30	265	106 ± 22	**6.6 ± 0.4**
CARGC02	5.26	45993	4745 ± 35*	4982		
CARGC06	5.00	45994	2590 ± 35*	2268	220 ± 45	6.0 ± 1
CARGC07	2.19	45988	2495 ± 35*	2163	99 ± 20	**
CARGC07	4.37	48029	3945 ± 30	4408		
CARGC09	0	48026	425 ± 30	195	148 ± 30	7.5 ± 1.5
CARGC09	2.13	48027	1535 ± 30	1439		
CARGC10	2.68	45989	2175 ± 30*	1770	151 ± 31	17.4 ± 3.4
CARGC13	4.93	48031	2515 ± 30	2591	190 ± 39	5.5 ± 0.8
CARGC14	0	45997	350 ± 30*	Failure	57 ± 12	**9.3** ± 0.8
CARGC14	3.79	45996	6180 ± 45*	6618		
CARGC15	0.74	45991	955 ± 30*	551	146 ± 47	13.6 ± 3.5
CARGC15	3.16	48024	1600 ± 30	1477		
CARGC15	4.50	48033	2910 ± 30	3048		
CARGC16	1.95	45995	5190 ± 45*	5550	35 ± 8	**6.7** ± 0.5
CARGC17	3.71	48025	5010 ± 30	5741	65 ± 13	9.2 ± 0.9
CARGC18	4.82	48032	2095 ± 30	2067	233 ± 47	6.7 ± 1.2

weighting each intermediate rate by the time-lapse over which it was measured. The corresponding uncertainty of the average sedimentation rate was then computed using the standard (total differentiation) uncertainty computation method. The relative uncertainty was an average of 20% for all four cores, which led us to apply a minimum relative uncertainty of 20% on the average sedimentation rate for all cores. The results are summarized in Table 2.

The ages at the base of the wedge were then either extrapolated to the core base or extrapolated to the wedge base on seismic profiles. In both cases, the wedge top depth and wedge base depth were obtained using very-high-resolution seismic profiles, with the uncertainty of those values ranging between 43 and 122 cm depending on the considered core. For two cores (CARG01 and 16), the base of the wedge was reached so that the bottom wedge age could be measured directly using core sedimentation rates (Table 2). For the cores that did not reach the bottom of the wedge (CARGC02, 06, 09, 10, 13, 14, 15, 17 and 18), the bottom wedge age was extrapolated by using its average sedimentation rate and measuring the distance between the last ^{14}C measurement and the bottom wedge. Here, again, the standard (total differentiation) method previously described was used to compute the uncertainty on the bottom wedge edge, but we also took into account the uncertainties due to ^{14}C measurements in the distance between this last measurement and the bottom wedge, as well as the uncertainty in the average sedimentation rates.

4. Results

4.1. Uppermost slope morphology

The very high-resolution profiles selected for this study show that the wedge mainly presents a transparent echofacies (Figs. 3, 4, 6 and 7). However, on a few profiles, the wedge echofacies shows low-amplitude laminations (Figs. 5 and 7). The wedge thickness is not constant along a downdip direction. The thickest parts are located on depressions of the Pleistocene substratum on the upper wedge.

4.2. Core lithology

The grain-size analyses of the cores show that the cores can contain three main grain-size ranges. The finest mode of particle grain-size ranges between 0.2 µm and 20 µm and is most abundant in cores CARGC01, CARGC02, CARGC06, CARGC09, CARGC15, CARGC16 and CARGC18 (Figs. 3–7; Table 1). Smear slide analyses show that this size range is mainly composed of particles produced on the platform (~78%; aragonite needles), those of undetermined origin (~22%; calcite crystals) and those produced in the water column (> 0.1%; coccoliths).

The second grain-size mode extends from 20 to 150 µm (silt to very fine sand). This grain-size range is dominant in cores CARGC10, CARGC13, CARGC14 and CARGC17 (Figs. 5–7; Table 1). Component analysis shows that this sediment mode is mainly composed of elements of undetermined origin (~72%, bioclasts, manganese and small iron nodules), those produced on the platform (~12%; crustaceans, gastropod and bivalve pieces, small pellets, broken *Halimeda* flakes, algae debris, and aggregates), those produced on the slope (~9%; corals from the external shelf edge, bryozoans, crinoid and echinoderm pieces, juvenile and adult benthic foraminifera, ostracods, and sponge spicules), and those produced in the water column (~7%; juvenile planktonic foraminifera and pteropods).

The last and coarsest mode (> 150 µm) shows the same composition as the 20–150 µm modes, but its foraminifera and pteropods are represented by adult forms, *Halimeda* flakes are whole and pellets are larger. According to grain size measurements and sieving results, this mode is dominant in cores CARGC07 (~60% of core grain size; Table 1). This core contains fewer aragonite needles (~13% of content) than other cores (mean value of ~32%). This core is located at the Cut 2 outlet (Fig. 2). For other cores, this mode is not or almost not represented (from 4 to 9%; Table 1), except in cores CARGC15 (~19% of core grain size; Table 1) and CARGC18 (~18% of core grain size; Table 1), which are, respectively, the shallowest cores of transect 4 and transect 5.

Currently, the sites located in the eastern part of the study area (transect 5) seem richer in water column elements (Fig. 7) than the sites located along other transects.

Most of the counted grains in the cores correspond to platform-derived sediments (~47% of total counted grains). The relative importance of platform grains in cores is mainly due to the high amount of aragonite needles. The percentage of aragonite needles increases from the shallowest cores to the deepest cores (Figs. 3–7), probably because coarser-grained modes are more abundant in the shallowest cores.

The second main group of sediments is composed of grains of undetermined origin (~31% of total counted grains). The third group is

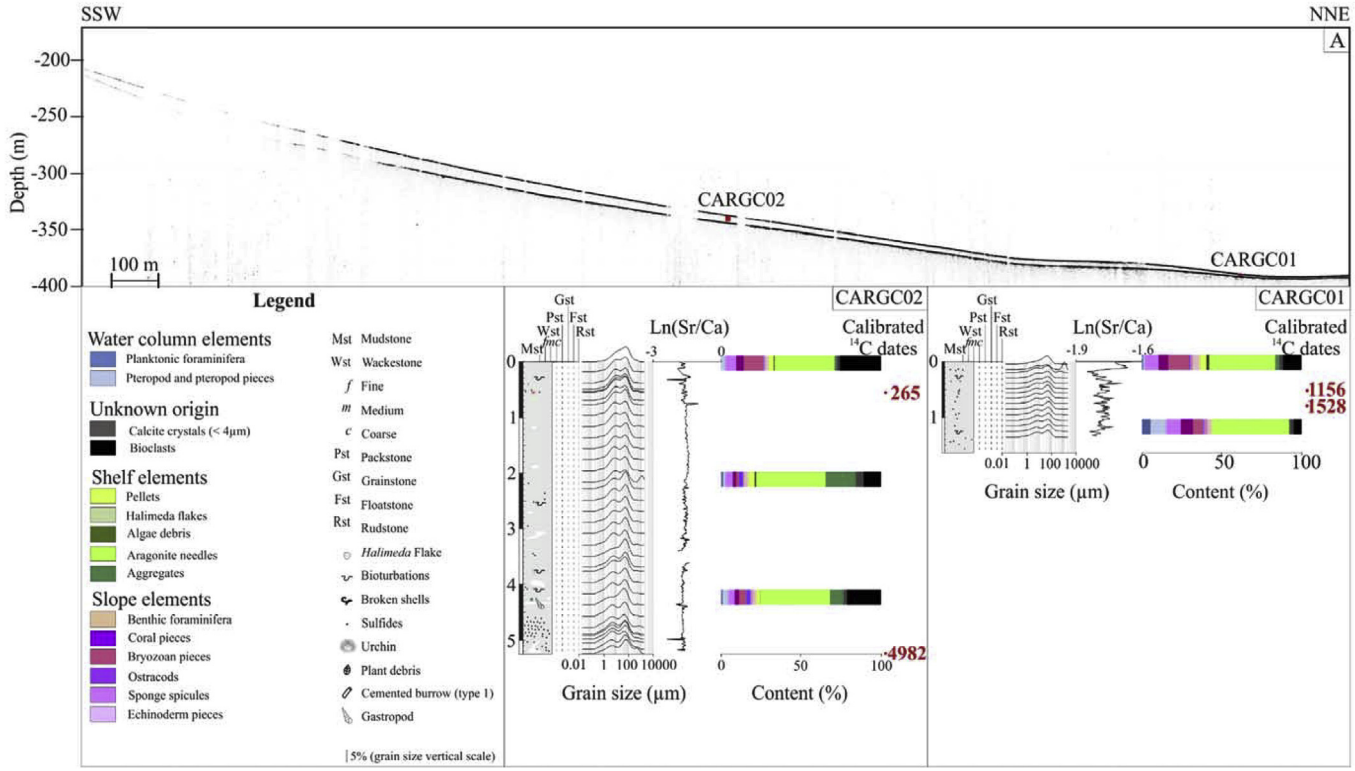

Fig. 3. Transect 1. Seismic profile (localization in Fig. 3) and lithology of cores CARGC01 and CARGC02. Calibrated radiocarbon ages are indicated in red. Grain size measurements (similar for Figs. 4–8) are indicated on the legend. (For interpretation of the references to colour in this figure legend, the reader is referred to the Web version of this article.)

composed of slope sediments (~17% of total counted grains), and the last group is formed by water column grains (~5% of total counted grains).

In core CARGC09, two laminated sequences (Figs. 3 and 8) were observed. Decile 50 (D50) and grain-size distribution highlight a rough coarsening-upward and then fining-upward trend, but in detail (Fig. 8), laminations are composed of an alternation of fine-grained (enriched in carbonate mud) and coarse-grained laminae (enriched in benthic foraminifera, bryozoan pieces, sponge spicules and pellets). Hence, those sequences are composed of the same elements as the wedge but enhanced in either the finest or coarsest modes. In both sequences, the basal coarse layers are not erosive but sharp, and coarse-grained

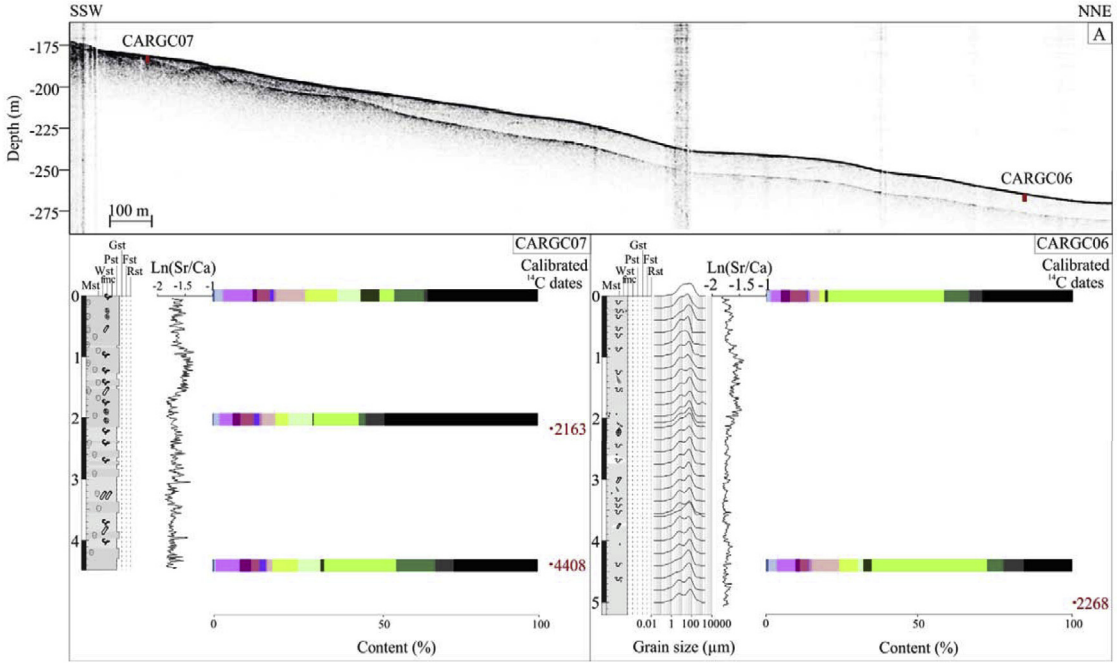

Fig. 4. Transect 2. Seismic profile (localization in Fig. 3) and lithology of cores CARGC06 and CARGC07. Calibrated radiocarbon ages are indicated in red (see legend in Fig. 3). (For interpretation of the references to colour in this figure legend, the reader is referred to the Web version of this article.)

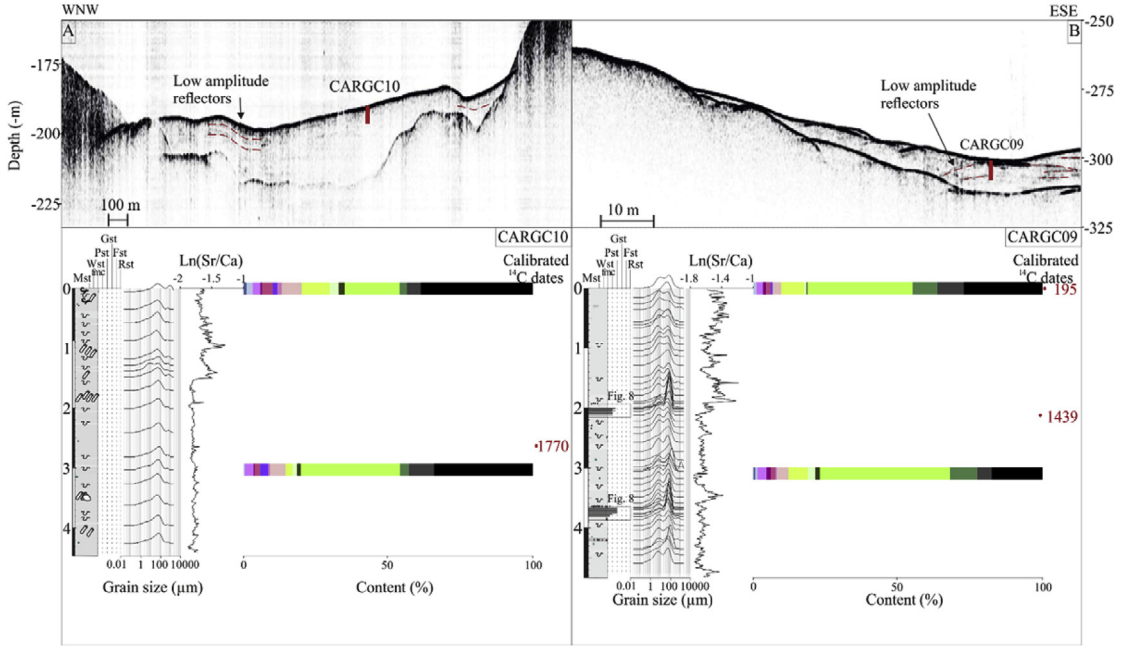

Fig. 5. Transect 3. Seismic profile (localization in Fig. 3) and lithology of cores CARGC09 and CARGC10. Calibrated radiocarbon ages are indicated in red (see legend in Fig. 3). (For interpretation of the references to colour in this figure legend, the reader is referred to the Web version of this article.)

laminae still contain little mud between grains (Fig. 8). The coarse-grained laminae thickness increases slightly upward (~1 mm thick for basal laminae) until it reaches a maximum thickness of > 1 cm. The coarse-grained laminae thicker than 1 cm are depleted in mud. Toward the top of the sequences, the thickness of the coarse-grained laminae slightly decreases and the carbonate mud content increases. The top coarse-grained layers are also not erosive, but sharp. Although both sequences are visually similar, the coarse laminae at the top of the older sequence (364–384 cm, Fig. 8) are thicker.

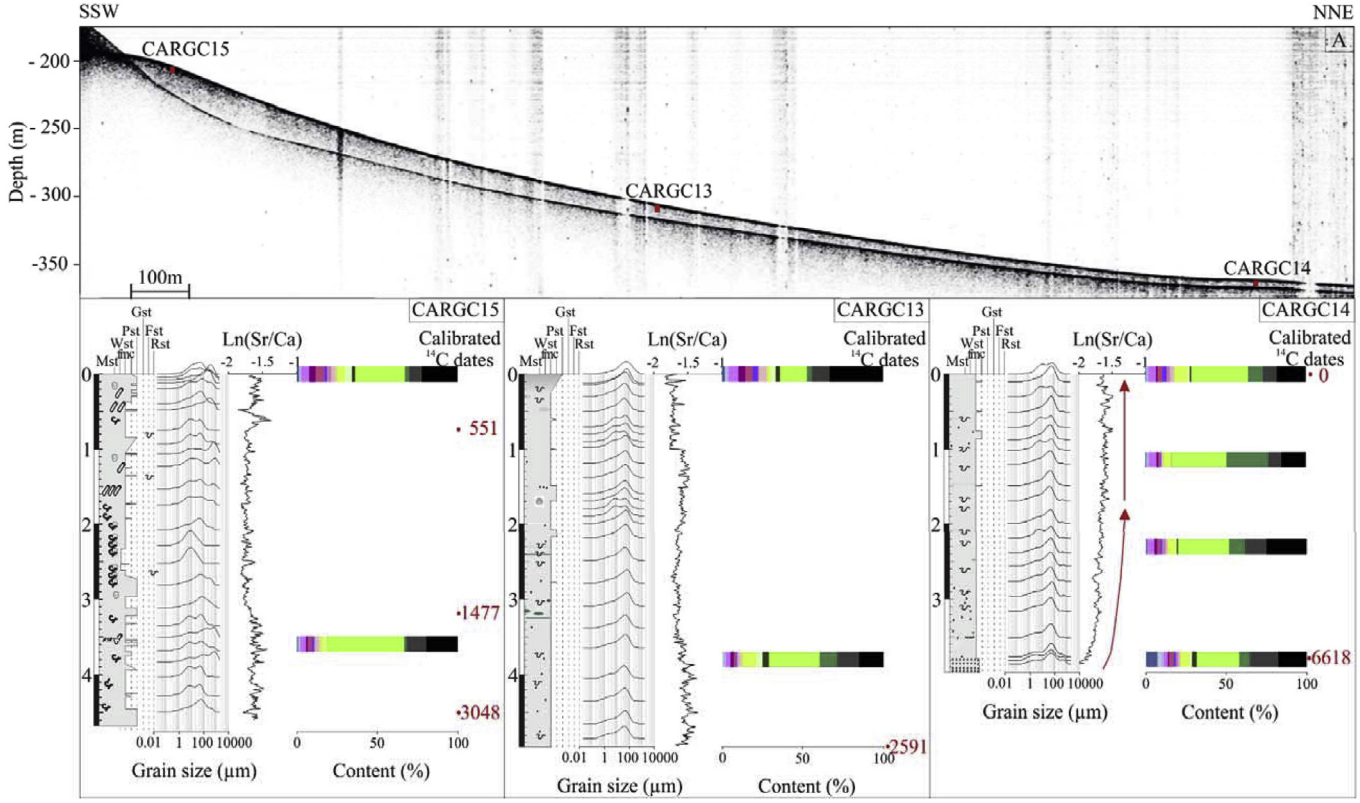

Fig. 6. Transect 4. Seismic profile (localization in Fig. 3) and lithology of cores CARGC13, CARGC14 and CARGC15. Calibrated radiocarbon ages are indicated in red (see legend in Fig. 3). (For interpretation of the references to colour in this figure legend, the reader is referred to the Web version of this article.)

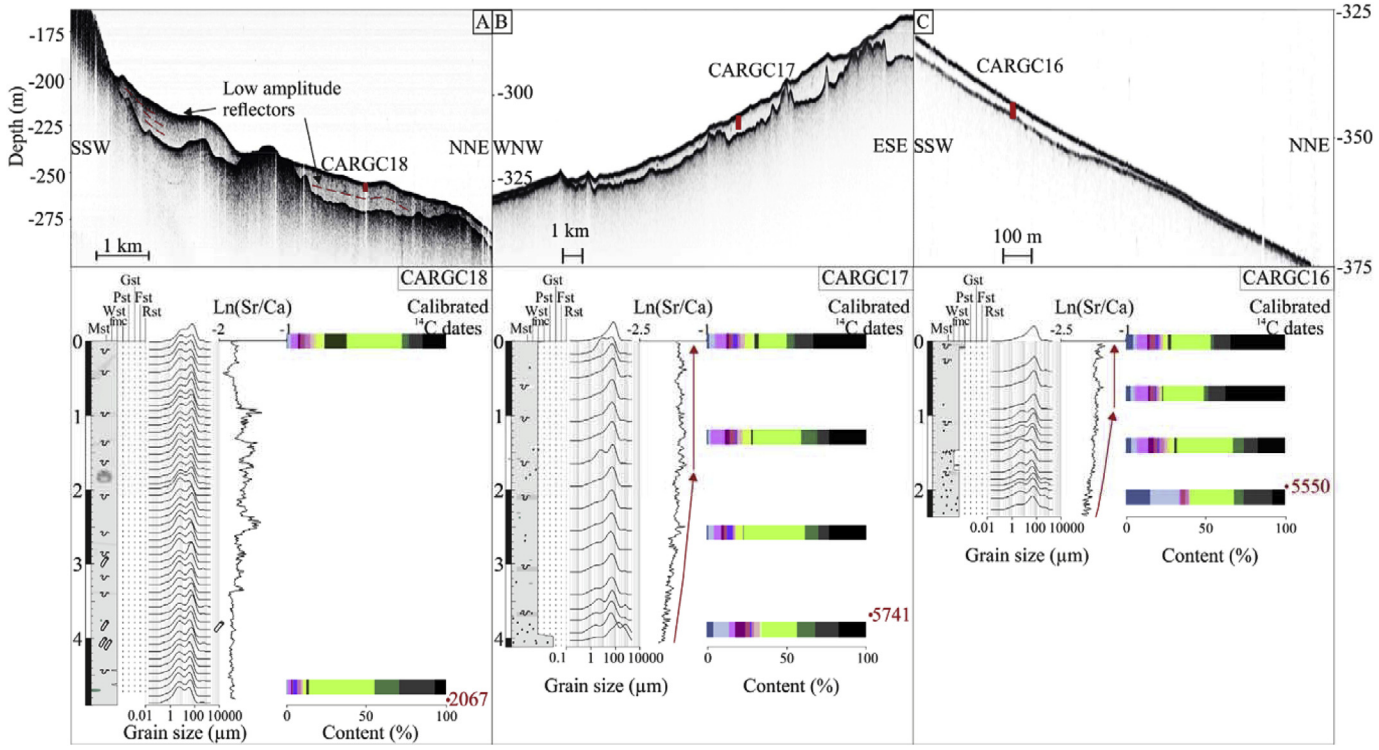

Fig. 7. Transect 5. Seismic profile (localization in Fig. 3) and lithology of cores CARGC16, CARGC17 and CARGC18. Calibrated radiocarbon ages are indicated in red (see legend in Fig. 3). (For interpretation of the references to colour in this figure legend, the reader is referred to the Web version of this article.)

4.3. Core stratigraphy and estimation of the age of wedge initiation

The measurements and calibrations of ages allowed the elaboration of an age model and the calculation of sedimentation rates for each core. The radiocarbon dates used for this study are summarized in Table 2. For the CARGC14 top, a non-calibrated age was obtained (350 yrs BP), but this age was not valid after calibration because the core top was dated post 1950 AD. We thus assume that very recent sediments form the core top. Except for transect 4 (Fig. 9), the highest sedimentation rates are found on the upper part of the wedge. There is no significant difference in the sedimentation rates between the eastern and western parts of the wedge in the study area (Fig. 9). Using the extrapolated and measured age values of the wedge bottom, we observe that the wedge supply was diachronous. The results (Fig. 9) show that: (1) 1 core located on the lower wedge (CARGC01, transect 1) shows wedge formation at 4.4 ± 0.8 kyr cal BP; (2) 6 cores located on the upper wedge (CARGC18, transect 5; CARGC02, transect 1), middle wedge (CARGC13, transect 4) and lower wedge (CARGC09, transect 3; CARGC06, transect 2; CARGC16, transect 5) show that wedge formation began between 5.5 ± 0.8 kyr cal BP and 7.5 ± 1.5 kyr cal BP; (3) 2 cores located on the lower (CARGC14, transect 4) and middle wedge (CARGC17, transect 5) show that wedge formation started approximately 9.25 ± 0.85 kyr cal BP; (4) 1 core located on the upper wedge (CARGC15, transect 4) reflect wedge formation around 13.6 ± 3.5 kyr cal BP; and (5) 1 core located on the upper wedge (CARGC10, transect 3) shows wedge formation occurring around 17.4 ± 3.4 kyr cal BP. This core is located in a topographic trough, suggesting a preferential infilling and high sedimentation rates at the beginning of wedge formation. As the core records only the top of the wedge, the sedimentation rates are largely underestimated. This age is probably too old, and this value has been discarded in this study.

Hence, the main supply started at 6.5 ± 0.9 kyr cal BP. This age is the average age obtained for 6 cores (CARGC02, CARGC06, CARGC09, CARGC13, CARGC16, and CARGC18), especially in core CARGC16, which was sampled from the base of the wedge.

The first deposition of the wedge using core transects perpendicular to the margin allows the study of wedge accommodation. These results show a global progradation on transects 1 and 3, and an aggradation on transects 4 and 5, as indicated in Fig. 9.

4.4. Evolution of deposition on the wedge

The cores that sampled the entire or a large part of the wedge exhibit a base enriched in sulfides and grey diagenetic aggregates and bioclasts (CARGC02, CARGC14, CARGC16, and CARGC17).

The XRF results did not show large variations of Sr and Ca, which are the main elements measured in cores, except for core CARGC09 (above the 2 laminated sequences) and core CARGC10 (on cemented burrows), where they are related to bioturbations. However, the Sr/Ca ratios of the three cores that have reached ~6 kyr cal BP (CARGC14, CARGC16, and CARGC17) widely increase from the base to core depth corresponding to ~2 kyr cal BP (Figs. 6 and 7). These cores have sampled the entire (CARGC16) or almost the entire (CARGC14, CARGC17) wedge, highlighting the progressive appearance of the platform signature on the western part of the wedge during the Holocene, especially at ~6 kyr cal BP. Grain content analyses are consistent with this ratio variation: the bottoms of western cores CARG14, CARGC16 and CARGC17 exhibit high contents of grains that formed in the water column (11%, 33% and 14%, respectively; deposition between 6 and 6.5 kyr cal BP in Figs. 6 and 7). On the eastern part of the wedge, other cores sampled the entire (CARGC01) or almost the entire wedge (CARGC02 and CARGC07), but records are limited to the last 5 kyr cal BP and do not show the increase of this ratio (Figs. 3 and 4). For this period, only few grains that formed in the water column are observed (respectively 5% and 1%; Figs. 3 and 4). The bottom of core CARGC01 (~2 kyr) is richer in grains that formed in the water column (15%) than other cores.

The content evolution shows that contents of aragonite needles are correlated with the age of samples. According to the ^{14}C results and sedimentation rate extrapolation, the aragonite needle content

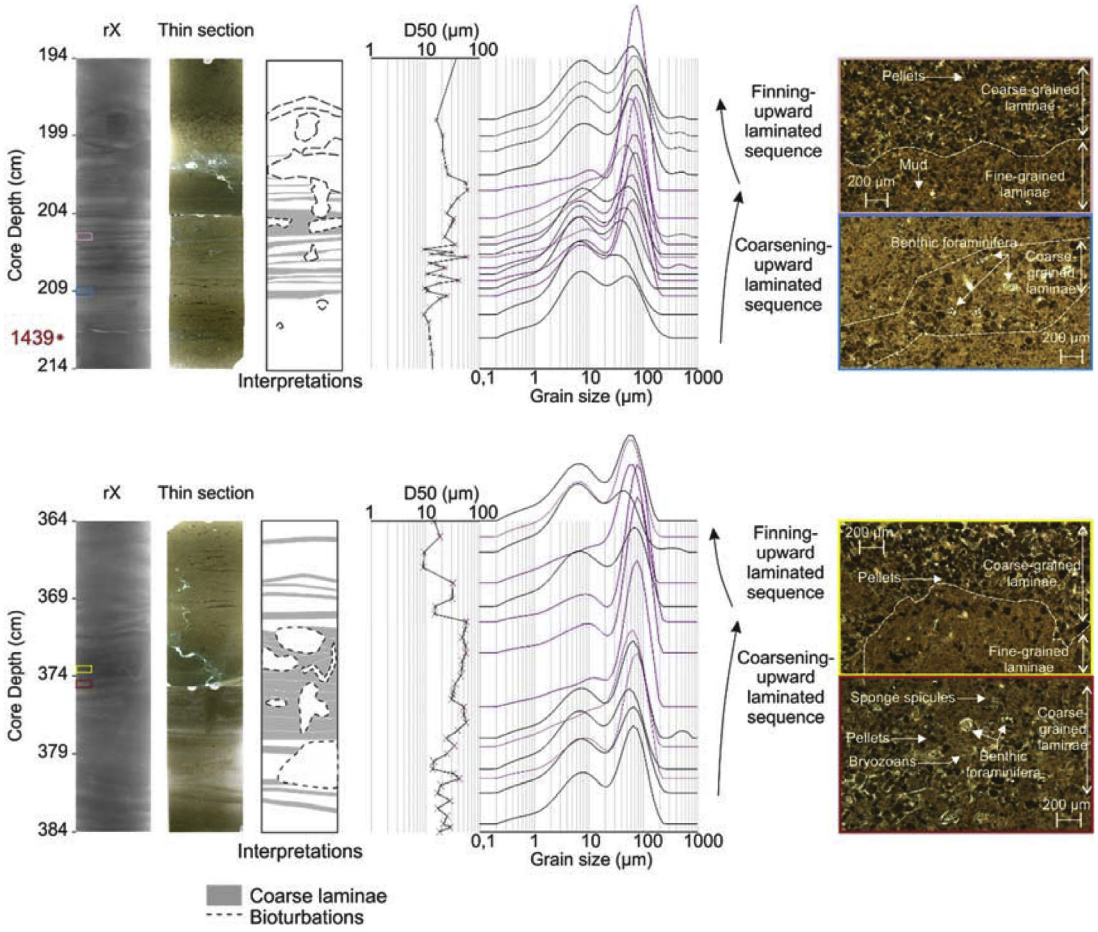

Fig. 8. Details of the laminated sequences found in core CARGC09. Coarse laminations are highlighted in purple on D50 and grain-size measurement results. Radiocarbon age (cal BP) is indicated by the red star on the right side. (For interpretation of the references to colour in this figure legend, the reader is referred to the Web version of this article.)

increases in cores between ~6 kyr cal BP and ~4 kyr cal BP (Figs. 3, 4 and 7) and then decreases since the last 4 kyr cal BP (Figs. 3–7).

5. Discussion

5.1. Which process is responsible of the Holocene wedge sediment supply?

In an isolated carbonate system, the uppermost slope is the critical zone connecting the carbonate platform and the open ocean. Therefore, the sediment composition is dominated by the grains formed and exported from shallow environments but also to a lesser extent from the slope and the water column.

Before the sea level reached the platform margin and prior to the entire flooding of the platform, “platform-derived grains” are produced and exported from uppermost slope terraces that act as small factories for the production of shallow environments.

The abundance of platform-related grains in cores is due to the high export of mud-size particles. Flume experiments (Schieber et al., 2013) have shown that carbonate mud can be transported by different processes according to either high (> 0.25 m/s) or low (< 0.25 m/s) velocities. Consequently, fine-grained particles can be exported at any flow velocity. The main grain types found in these samples correspond to grains formed on the platform, suggesting an export process coming from the platform strong enough to cross the platform edge. Moreover, this process can carry sediments to the uppermost slope and be energetic enough to export peloids to the slope (Chabaud et al., 2015; Tournadour et al., 2017) but is unable to transport ooids, because particle composition analysis revealed that no ooid is present on the uppermost slope core samples. This supports Hine's (1977) hypothesis: tidal currents along the northern LBB are not sufficiently widespread to cause the wholesale movement of sand bodies, and seagrass stabilizing ooid shoals also prevents mobilization. Those features prevent a supply from ooid shoals to the Holocene wedge. The tidal current velocity is enhanced to 1 m/s when the tidal flux is confined in cuts between cays, but as soon as the wet section increases, the tidal flow velocity drops down and coarser particles settle in ebb tidal deltas. However, if re-suspension is important on the platform during other remobilizing processes, tidal currents can reach sufficient velocities to help export sediments (< 0.5 mm) mobilized by other phenomena. Consequently, it is necessary for the velocity of the export process to be lower than 0.4 m/s, which represents the velocity threshold to initiate the motion of 0.4- to 0.5-mm diameter ooids (Reeder and Rankey, 2009). In addition, the process must be able to export fine-grained particles along the entire platform margin. The re-suspension of sediment increased during cold fronts associated with hyperpycnal cascades along the platform margin could export sediments to the slope through the process of density cascading (Wilson and Robert, 1995).

The laminated sequences found in core CARGC09 could be a clue for decrypting the hydrodynamic conditions of the processes that supply the wedge. As CARGC09 is located in a depression with high sedimentation rates, these sequences could be better preserved than in cores located on the slope, and their presence may not be due to a particular local sedimentary environment. Parallel laminae can result either from a decantation process or could be tractive structures resulting from a turbulent depositional lower planar flow regime. The lack of erosion on the bases of coarse-grained laminae suggests

continuous and quasi-steady processes. A paucity of bioturbation suggests a quite high sedimentation rate. The energy of the depositional process related to these sequences probably increases progressively until reaching a velocity peak with values high enough to winnow the finest particles. After reaching the peak, the velocity decreases. However, the duration of the deposition of a whole sequence is hard to determine. In this core, only 40 cm of laminated sequences were found over the 4.8 m of the core. These sequences are probably due to rare events. The winnowing of mud in the middle of the sequence and rare bioturbations are probably due to a high-energy process. Coarsening and fining-upward sequences can be interpreted as the result of the variation in hurricane intensity along a single event with a pathway close to the study area that generates the mobilization of platform grains as observed on the coarse-grained layers. Hurricanes are very high-energy events common in this area that can resuspend and export platform grains as benthic foraminifera in the lagoons and generate peaks in coarse-grained sequences as described by Toomey et al. (2013). The turbidity in a lagoon is maximal after each hurricane passage (Fig. 1). In this case, the laminated sequence would represent the fall-out of carbonate mud exported from the platform during a hurricane with its energy first increasing and then decreasing. On the other hand, hurricanes can also resuspend fine-grained particles on the uppermost slope down to a water depth of 150 m. For example, recent simulations highlighted that hurricane Matthew (Fig. 1) managed to disturb the Florida Current boundary layer from 200 mbsl to 500 mbsl (Ezer et al., 2017). These observations were made at a range of water depth that includes the water depth of the Holocene wedge on the LBB. Consequently, energetic water mass movements bringing sediments can happen on the upper slope. The sequences would then represent very low-density turbulent flow supplies by the seafloor mud resuspension during the waxing and waning phases of hurricane intensity variations. If the interpretation of coarsening and fining-upward sequences is correct, the presence of only two lamina sequences suggests that hurricanes represent only a minor process in wedge supply, especially because of their variable pathways.

5.2. Spatial sedimentation model of the Holocene wedge

The coarsest grains are concentrated along the upper part of the wedge whilst mud is exported in deeper water, even on the slope below 300 mbsl (Chabaud et al., 2015). This observation is confirmed over the whole study area according to grain size measurements of all of the cores. This sorting is particularly efficient at cut outlets, where no barriers retain the current. There, tidal currents can also induce a large range of flow velocity, emphasizing the sorting process. Seaward of cuts, the Pleistocene substratum is eroded by small channels, suggesting the high velocities and charge of currents (Fig. 2). This higher velocity of flows may be at the origin of a better elutriation and a higher coarse-grain concentration below cut outlets than anywhere, as demonstrated by the grain size differences between the upper wedge cores located below cuts and those not located below cuts.

5.3. Evolution of Holocene wedge deposition

The sedimentation rates calculated using core age models (35–233 cm/kyr, Table 2) are 6–40 times lower than those found on the GBB wedge at comparable water depths (11–15 m/kyr; Wilber et al., 1990), which is the expected difference between a windward and a leeward margin.

Although the initial deposition time at the base of the wedge is difficult to determine, our data show that the wedge was initiated at different times and supplied at different periods. Initial deposition started around 13.6 ± 3.5 kyr cal BP (Fig. 9), after the meltwater pulse 1 A (MWP1A, ~14 kyr cal BP; Fig. 10; Deschamps et al., 2012; Liu et al., 2004; Liu and Milliman, 2004; Zecchin et al., 2015). A meltwater pulse is an acceleration in sea-level rise that results from outbursts of pro- or subglacial meltwater and/or surging of ice-streams into the ocean during ice sheet disintegration (Hopley, 2011). Meltwater pulses have impacted upper slopes everywhere in the world (Bard et al., 2010; Deschamps et al., 2012; Fairbanks, 1989; Liu et al., 2004; Liu and Milliman, 2004; Zecchin et al., 2015). During its initial phase, the wedge probably only filled shallow depressions in the Pleistocene substratum: these depressions trapped particles mainly formed along the slope and in the water column, and shallow environment-derived particles could be produced on terrace 4 (T4; 55–64 mbsl; Fig. 10) described by terraces would be formed during periods of standing sea-level that have occurred since the Last Glacial Maximum and would either correspond to a period of coral reef settlement or/and a flooding surface flattened by wave breaking and other shallow energetic hydrodynamic processes (stillstand and ravinement surfaces). After periods of meltwater pulses and induced rising sea-level, the erosion of the terrace and enhanced carbonate production on these flooded flat shallow areas would explain the increase in wedge formation. Terraces T3, T2 and T1 formed after MWP1B (~11.5 kyr cal BP; Lambeck et al., 2011; Liu et al., 2004; Liu and Milliman, 2004, Fig. 10) and possibly after mpw1c (9–9.5 kyr cal BP; Fig. 10 Liu et al., 2004, Fig. 10). They could have supplied the growing wedge dated in our study at 9.25 ± 0.85 kyr cal BP (Fig. 10). During the early period of wedge formation, this scenario is highly consistent with the uppermost slope morphology described by Rankey and Doolittle (2012) and Mulder et al. (2017), which supposed that the uppermost slope morphology was impacted by sea-level stillstands.

The main period of wedge growth started around 6.5 ± 0.9 kyr cal BP (Fig. 9; Roth and Reijmer, 2004), when sea-level reached the LBB margins. The western area that sampled this period is characterized by a larger proportion of water column-related particles, and a few diagenetized grains are mixed with these particles (Fig. 7). Around 6 kyr cal BP, the wedge supply began to get enriched by platform-derived sediments (Fig. 10).

From ~6 kyr cal BP to ~4 kyr cal BP, the platform was flooded with

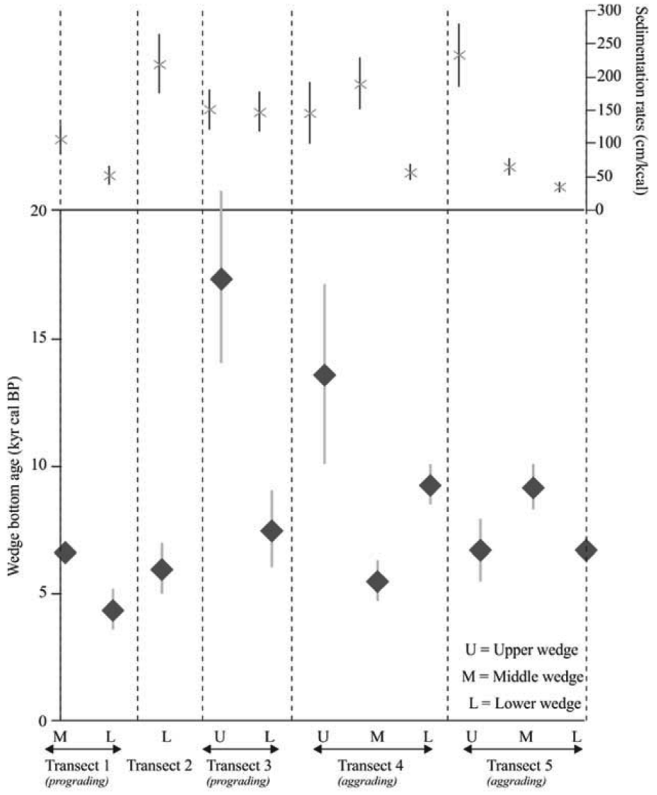

Fig. 9. Uncertainties of sedimentation rates and wedge bottom ages.

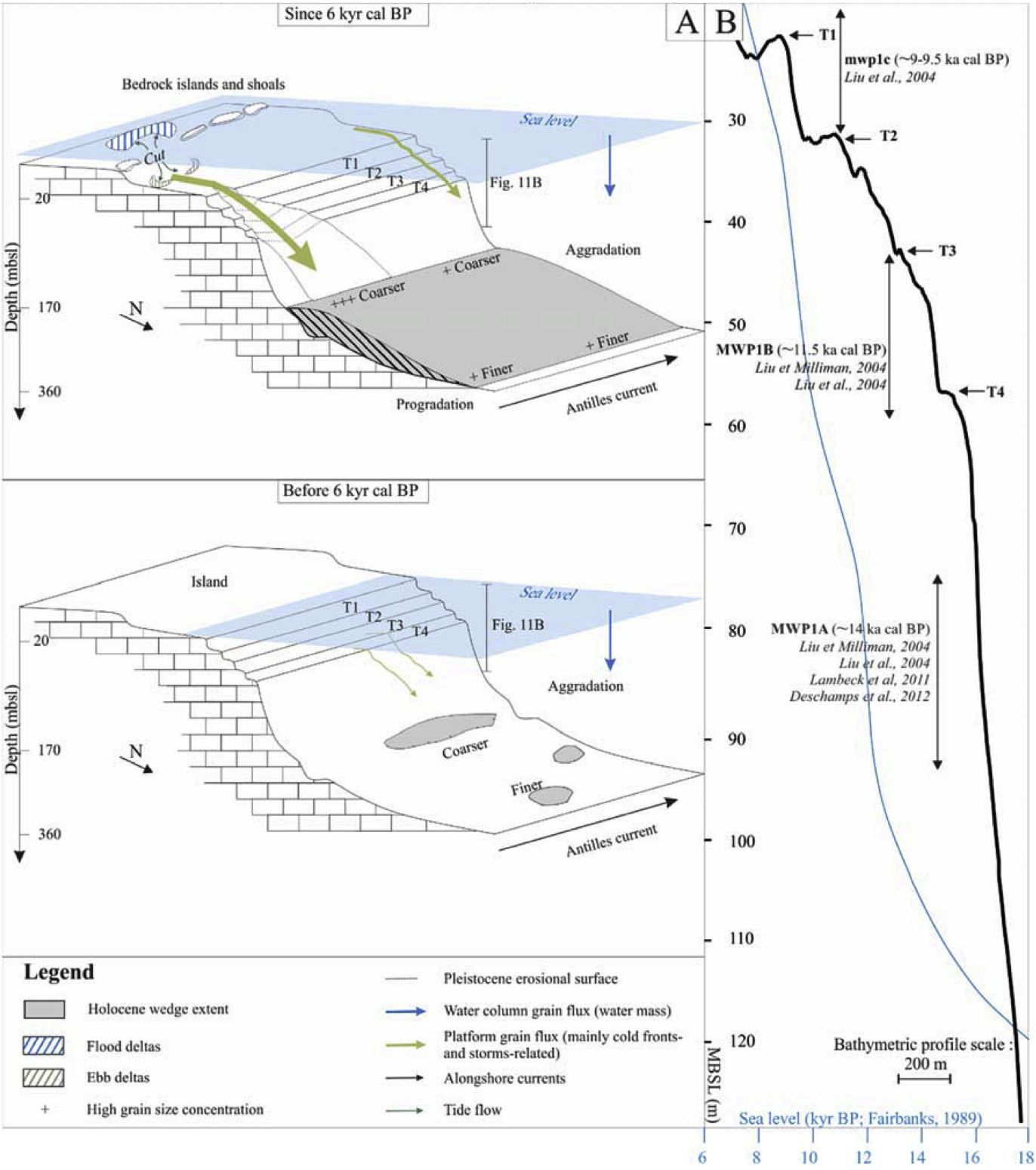

Fig. 10. A: Conceptual scheme of sediment export along the LBB margin during the Holocene. This scheme highlights the coarse-grained sediments that were more abundant on the upper wedge and the fine-grained sediments on the lower wedge that supplied Pleistocene depressions before 6 kyrs BP. B: Bathymetric profile (in black) between the platform edge and the wedge (location in Fig. 2) showing the main terraces and their link with meltwater pulses. Barbados sea level (in blue; Fairbanks, 1989) is plotted on Fig. 10B. (For interpretation of the references to colour in this figure legend, the reader is referred to the Web version of this article.)

a maximum at 4.4 kyr cal BP according to Ramsay (1996), Ramsay and Cooper (2002) and Roth and Reijmer (2004). In our cores, this maximum flooding period around 4 kyr cal BP is characterized by the maximum export of platform-derived particles (mainly aragonite needles (Figs. 3–7)).

The period between ~4 kyr cal BP and present day corresponds to a global decrease of ~3 m in sea level along Caribbean coasts (Ramsay and Cooper, 2002), illustrated by a decrease in the aragonite needle content.

These observations suggest a narrow link between sea-level

variations during the Holocene (*e.g.,* meltwater pulses and maximum flooding), uppermost slope morphology (terraces that supply the wedge at its initial deposition) and wedge supply (variations in wedge contents and sedimentation rates).

6. Conclusions

This detailed study of core transects collected along the LBB Holocene wedge allowed the interpretation of the processes that supplied this sedimentary body. Our results of particle identification and radiocarbon ages allowed the discussion of the sedimentary process feeding the wedge sediment and the variations of productivity it has recorded.

(1) The LBB wedge is mainly built by density cascading processes generated after the arrival of winter cold fronts, allowing for seasonal export from the lagoons all along the platform. Hurricanes and storms can sporadically contribute to wedge supply by increasing the mobilization of sediments on the platform, and, depending on the conditions, their export to the wedge. Tide-related currents are not strong enough to mobilize platform sediments, but they may also participate in wedge export by helping the slopeward motion of sediments previously mobilized by hurricanes and cold fronts. The local morphology of the platform edge allows for the better sorting and export of sediments according to the presence of outlets.
(2) The wedge initiation started after the meltwater pulse 1 A (13.6 ± 3.5 kyr cal BP). It was first supplied by the shallow environment productivity of four narrow terraces after MWP1A, MWP1B and mwp1c. The main period of wedge growth started around 6.5 ± 0.9 kyr cal BP, when sea level reached the present platform margins. The maximum flooding period around 4 kyr cal BP is characterized by the maximum export of platform-derived particles (mainly aragonite needles).

This periplatform wedge was mainly supplied during the Holocene, but its initiation probably started during the last termination. These results demonstrated that the Bahamas have recorded the last meltwater pulses in a way similar to many sites located all over the world. The terraces created by those meltwater pulses may have acted as shallow environments able to export sediments offshore.

Acknowledgements

The authors thank the captain and crew of the R/V F.G. Walton Smith for the quality of the acquired data and the Rosenstiel School of Marine and Atmospheric Sciences for their help in cruise organization. Multibeam data acquisition was supervised by Cody Carlson (Seafloor System Inc.). This work is supported by the French INSU program “Actions Marges” and was sponsored by the TOTAL Research laboratory. K. Fauquembergue's Ph.D. Grant was also funded by TOTAL. We would like to thank the program ARTEMIS for radiocarbon date analyses. We also thank Mickael Grech (LULI, CNRS, Ecole Polytechnique, CEA, Université Paris-Saclay, Sorbonne Université, Palaiseau, France) for his valuable help concerning the uncertainty calculations. We also would like to thank the two anonymous reviewers for their pertinent remarks, which clearly improved this paper.

References

Bard, E., Hamelin, B., Delanghe-Sabatier, D., 2010. Deglacial meltwater pulse 1B and younger dryas sea levels revisited with boreholes at tahiti. Science 327, 1235–1237. https://doi.org/10.1126/science.1180557.

Betzler, C., Lindhorst, S., Eberli, G.P., Ludmann, T., Mobius, J., Ludwig, J., Schutter, I., Wunsch, M., Reijmer, J.J.G., Hubscher, C., 2014. Periplatform drift: the combined result of contour current and off-bank transport along carbonate platforms. Geology 42, 871–874. https://doi.org/10.1130/G35900.1.

Boardman, M.R., 1988. Holocene Sea Level in the Bahamas, J. E. Mylroie. Bahamian Filed Station.

Chabaud, L., Ducassou, E., Tournadour, E., Mulder, T., Reijmer, J.J.G., Conesa, G., Giraudeau, J., Hanquiez, V., Borgomano, J., Ross, L., 2015. Sedimentary processes determining the modern carbonate periplatform drift of Little Bahama Bank. Mar. Geol. https://doi.org/10.1016/j.margeo.2015.11.006.

Croudace, I.W., Rindby, A., Rothwell, R.G., 2006. ITRAX: description and evaluation of a new multi-function X-ray core scanner. Geol. Soc. Lond. Spec. Publ. 267, 51–63.

Deschamps, P., Durand, N., Bard, E., Hamelin, B., Camoin, G., Thomas, A.L., Henderson, G.M., Okuno, J., Yokoyama, Y., 2012. Ice-sheet collapse and sea-level rise at the Bølling warming 14,600 years ago. Nature 483, 559–564. https://doi.org/10.1038/nature10902.

Droxler, A.W., 1983. Late Quaternary Glacial Cycles in the Bahamian Deep Basins and in the Adjacent Atlantic ocean. University of Miami, Coral Gables, Florida.

Enos, P., 1974. Map of Surface Sediment Facies of the Florida-Bahamas Plateau.

Ezer, T., Atkinson, L.P., Tuleya, R., 2017. Observations and operational model simulations reveal the impact of Hurricane Matthew (2016) on the Gulf Stream and coastal sea level. Dynam. Atmos. Oceans 80, 124–138. https://doi.org/10.1016/j.dynatmoce.2017.10.006.

Fairbanks, R.G., 1989. A 17,000-year glacio-eustatic sea level record: influence of glacial melting rates on the Younger Dryas event and deep-ocean circulation. Nature 342, 637–642. https://doi.org/10.1038/342637a0.

Gischler, E., Dietrich, S., Harris, D., Webster, J.M., Ginsburg, R.N., 2013. A comparative study of modern carbonate mud in reefs and carbonate platforms: mostly biogenic, some precipitated. Sediment. Geol. 292, 36–55. https://doi.org/10.1016/j.sedgeo.2013.04.003.

Glaser, K.S., Droxler, A., 1991. High production and highstand shedding from deeply submerged carbonate banks, northern Nicaragua rise. J. Sediment. Petrol., SEPM 61, 128–142.

Hardy, J., Henderson, K., 2003. Cold front variability in the southern United States and the influence of atmospheric teleconnection patterns. Phys. Geogr. 24, 120–137. https://doi.org/10.2747/0272-3646.24.2.120.

Hine, A.C., Neumann, A.C., 1977. Shallow carbonate-bank-margin growth and structure, little Bahama Bank. Bahamas. AAPG Bull. 61, 376–406.

Hine, A.C., Wilber, R.J., Neumann, A.C., 1981. Carbonate sand bodies along contrasting shallow bank margins facing open seaways in northern Bahamas. AAPG Bull. 65, 261–290.

Hopley, D. (Ed.), 2011. Encyclopedia of Modern Coral Reefs, Encyclopedia of Earth Sciences Series. Springer Netherlands, Dordrecht. https://doi.org/10.1007/978-90-481-2639-2.

Johns, B., 2011. R/V Knorr Cruise KN-200-4 (Cruise Report). Port Everglades, FL to Port Everglades, FL.

Lambeck, K., Antonioli, F., Anzidei, M., Ferranti, L., Leoni, G., Scicchitano, G., Silenzi, S., 2011. Sea level change along the Italian coast during the Holocene and projections for the future. Quat. Int. 232, 250–257. https://doi.org/10.1016/j.quaint.2010.04.026.

Lantzsch, H., Roth, S., Reijmer, J.J.G., Kinkel, H., 2007. sea-level related resedimentation processes on the northern slope of little Bahama Bank (middle Pleistocene to Holocene). Sedimentology 54, 1307–1322. https://doi.org/10.1111/j.1365-3091.2007.00882.x.

Liu, J.P., Milliman, J.D., 2004. Reconsidering melt-water pulses 1A and 1B: global impacts of rapid sea-level rise. J. Ocean Univ. China, JOUC 3, 183.

Liu, J.P., Milliman, J.D., Gao, S., Cheng, P., 2004. Holocene development of the yellow River's subaqueous delta, north yellow sea. Mar. Geol. 209, 45–67. https://doi.org/10.1016/j.margeo.2004.06.009.

Meinen, C.S., Garzoli, S.L., Johns, W.E., Baringer, M.O., 2004. Transport variability of the deep western boundary current and the Antilles current off abaco island. Bahamas. Deep Sea Res. Part Oceanogr. Res. Pap. 51, 1397–1415. https://doi.org/10.1016/j.dsr.2004.07.007.

Migeon, S., Weber, O., Faugères, J.-C., Saint-Paul, J., 1998. SCOPIX: a new X-ray imaging system for core analysis. Geo Mar. Lett. 18, 251–255.

Mulder, T., 2014. Carambar 1.5 Cruise Report.

Mulder, T., Ducassou, E., Gillet, H., Hanquiez, V., Tournadour, E., Combes, J., Eberli, G.P., Kindler, P., Gonthier, E., Conesa, G., Robin, C., Sianipar, R., Reijmer, J.J.G., Francois, A., 2012. Canyon morphology on a modern carbonate slope of the Bahamas: evidence of regional tectonic tilting. Geology 40, 771–774. https://doi.org/10.1130/G33327.1.

Mulder, T., Joumes, M., Hanquiez, V., Gillet, H., Reijmer, J.J.G., Tournadour, E., Chabaud, L., Principaud, M., Schnyder, J.S.D., Borgomano, J., Fauquembergue, K., Ducassou, E., Busson, J., 2017. Carbonate slope morphology revealing sediment transfer from bank-to-slope (Little Bahama Bank, Bahamas). Mar. Petrol. Geol. 83, 26–34. https://doi.org/10.1016/j.marpetgeo.2017.03.002.

Mullins, H.T., Boardman, M.R., Neumann, A.C., 1979. Echo character of off-platform carbonates. Mar. Geol. 32, 251–268.

Mullins, H.T., Gardulski, A.F., Hine, A.C., Melillo, A.J., Wise, S.W., Applegate, J., 1988. Three-dimensional sedimentary framework of the carbonate ramp slope of central west Florida: a sequential seismic stratigraphic perspective. Geol. Soc. Am. Bull. 100, 514–533.

Ramsay, P.J., 1996. 9000 years of sea-level change along the southern African coastline. Quat. Int. 31, 71–75.

Ramsay, P.J., Cooper, J.A.G., 2002. Late quaternary sea-level change in South Africa. Quat. Res. 57, 82–90. https://doi.org/10.1006/qres.2001.2290.

Rankey, E.C., Doolittle, D.F., 2012. Geomorphology of carbonate platform-marginal uppermost slopes: insights from a Holocene analogue, Little Bahama Bank, Bahamas: uppermost carbonate platform slope, Bahamas. Sedimentology 59, 2146–2171. https://doi.org/10.1111/j.1365-3091.2012.01338.x.

Rankey, E.C., Enos, P., Steffen, K., Druke, D., 2004. Lack of impact of hurricane Michelle on tidal flats, Andros Island, Bahamas: integrated remote sensing and field observations. J. Sediment. Res. 74, 654–661.
Rankey, E.C., Reeder, S.L., 2011. Holocene oolitic marine sand complexes of the Bahamas. J. Sediment. Res. 81, 97–117. https://doi.org/10.2110/jsr.2011.10.
Rankey, E.C., Riegl, B., Steffen, K., 2006. Form, function and feedbacks in a tidally dominated ooid shoal. Bahamas. Sedimentol. 53, 1191–1210. https://doi.org/10.1111/j.1365-3091.2006.00807.x.
Reeder, S.L., Rankey, E.C., 2009. Controls on morphology and sedimentology of carbonate tidal deltas, Abacos. Bahamas. Mar. Geol. 267, 141–155. https://doi.org/10.1016/j.margeo.2009.09.010.
Reeder, S.L., Rankey, E.C., 2008. Interactions between tidal flows and ooid shoals, Northern Bahamas. J. Sediment. Res. 78, 175–186. https://doi.org/10.2110/jsr.2008.020.
Reimer, P.J., Bard, E., Bayliss, A., Beck, J.W., Blackwell, P.G., Ramsey, C.B., Buck, C.E., Cheng, Hai, Edwards, R.L., Friedrich, M., Grootes, P.M., Guilderson, T.P., Haflidason, H., Hajdas, I., Hatté, C., Heaton, T.J., Hoffmann, D.L., Hogg, A.G., Hughen, K.A., Kaiser, K.F., 2013. Intcal13 and Marine13 radiocarbon age calibration curves 0-50,000 Years cal bp. Radiocarbon 55, 1869–1887.
Rosenthal, Y., Boyle, E.A., Slowey, N., 1997. Temperature control on the incorporation of magnesium, strontium, fluorine, and cadmium into benthic foraminiferal shells from Little Bahama Bank: prospects for thermocline paleoceanography. Geochem. Cosmochim. Acta 61, 3633–3643.
Roth, S., Reijmer, J.J.G., 2004). Holocene Atlantic climate variations deduced from carbonate periplatform sediments (leeward margin, Great Bahama Bank): Holocene Atlantic climate variations. Paleoceanography 19. https://doi.org/10.1029/2003PA000885 n/a-n/a.
Schieber, J., Southard, J.B., Kissling, P., Rossman, B., Ginsburg, R., 2013. Experimental deposition of carbonate mud from moving suspensions: importance of flocculation and implications for modern and ancient carbonate mud deposition. J. Sediment. Res. 83, 1025–1031. https://doi.org/10.2110/jsr.2013.77.
Swart, P.K., Oehlert, A.M., Mackenzie, G.J., Eberli, G.P., Reijmer, J.J.G., 2014. The fertilization of the Bahamas by Saharan dust: a trigger for carbonate precipitation? Geology 42, 671–674. https://doi.org/10.1130/G35744.1.
Toomey, M.R., Curry, W.B., Donnelly, J.P., van Hengstum, P.J., 2013. Reconstructing 7000 years of North Atlantic hurricane variability using deep-sea sediment cores from the western Great Bahama Bank: a 7000 YR RECORD OF HURRICANE ACTIVITY. Paleoceanography 28, 31–41. https://doi.org/10.1002/palo.20012.
Tournadour, E., Mulder, T., Borgomano, J., Gillet, H., Chabaud, L., Ducassou, E., Hanquiez, V., Etienne, S., 2017. Submarine canyon morphologies and evolution in modern carbonate settings: the northern slope of Little Bahama Bank. Bahamas. Mar. Geol. 391, 76–97. https://doi.org/10.1016/j.margeo.2017.07.014.
Tournadour, E., Mulder, T., Borgomano, J., Hanquiez, V., Ducassou, E., Gillet, H., 2015. Origin and architecture of a Mass Transport Complex on the northwest slope of Little Bahama Bank (Bahamas): relations between off-bank transport, bottom current sedimentation and submarine landslides. Sediment. Geol. 317, 9–26. https://doi.org/10.1016/j.sedgeo.2014.10.003.
Traverse, A., Ginsburg, R.N., 1966. Palynology of the surface sediments of Great Bahama Bank, as related to water movement and sedimentation. Mar. Geol. 4, 417–459.
Wilber, R.J., Milliman, J.D., Halley, R.B., 1990. Accumulation of bank-top sediment on the western slope of Great Bahama Bank: rapid progradation of a carbonate megabank. Geology 18, 970–974.
Wilson, P.A., Robert, H.H., 1995. Density cascading: off-shelf sediment transport, evidence and implications, Bahama banks. SEPM J. Sediment. Res. 65A. https://doi.org/10.1306/D426801D-2B26-11D7-8648000102C1865D.
Zaragosi, S., Bourillet, J.-F., Eynaud, F., Toucanne, S., Denhard, B., Van Toer, A., Lanfumey, V., 2006. The impact of the last European deglaciation on the deep-sea turbidite systems of the Celtic-Armorican margin (Bay of Biscay). Geo Mar. Lett. 26, 317–329. https://doi.org/10.1007/s00367-006-0048-9.
Zecchin, M., Ceramicola, S., Lodolo, E., Casalbore, D., Chiocci, F.L., 2015. Episodic, rapid sea-level rises on the central Mediterranean shelves after the Last Glacial Maximum: a review. Mar. Geol. 369, 212–223. https://doi.org/10.1016/j.margeo.2015.09.002.
Zinke, J., Reijmer, J.J., Thomassin, B., 2003. Systems tracts sedimentology in the lagoon of Mayotte associated with the Holocene transgression. Sediment. Geol. 160, 57–79. https://doi.org/10.1016/S0037-0738(02)00336-6.